Heat Treatment Optimization of High-Pressure Die Casting Automotive Components Made in High Recycled AlSi10MnMg Alloy

ELENA MINGOTTI, LUCA GIRELLI, RICCARDO ARCALENI, LUCIA LATTANZI, MARIALAURA TOCCI, ALESSANDRO MORRI, and ANNALISA POLA

Aluminum alloys are widely used in automotive components due to their low density, which contributes to vehicle lightweighting and reduced CO_2 emissions, as well as their favorable mechanical properties. High-recycled-content alloys offer the potential to further enhance sustainability, however, the presence of recycled-related impurities, such as Fe, can influence microstructure and mechanical behavior, making it important to investigate their effects for automotive applications. This study explores whether high-quality, high-recycled-content AlSi10MnMg automotive casting, combined with tailored heat treatments (HTs), can achieve the performance targets required for specific structural automotive components. Comprehensive microstructural characterization (including optical microscopy, scanning electron microscopy, and electron backscatter diffraction) was combined with an extensive mechanical evaluation through hardness, tensile, bending, and self-piercing riveting tests to assess compliance with the required automotive performance standards.

https://doi.org/10.1007/s11661-026-08144-9

I. INTRODUCTION

THE reduction of the greenhouse gas emissions associated with the automotive sector is a key challenge in achieving global climate neutrality targets.[1,2] In this context, the transition from internal combustion engines to battery electric vehicles has accelerated in recent years, placing increasing emphasis on vehicle lightweighting as an effective strategy to reduce energy consumption and extend driving range. This goal can be achieved through appropriate material selection and process optimization, which represent critical levers for sustainable vehicle design.[3] Among lightweight materials, aluminum alloys play a central role in automotive applications due to their high specific strength, good formability, and excellent thermal and electrical conductivity. Compared to steel, aluminum enables mass reductions of up to 65 pct (resulting in lower-energy consumption and, therefore, in CO_2 emissions reduction), and improved performance of electric powertrains and thermal management systems.[4] Consequently, aluminum alloys are widely used in structural and functional components, including engine blocks, heat exchangers, battery housings, and structural frames and body in white parts.[5,6]

High-pressure die casting (HPDC) is one of the most established manufacturing routes for aluminum automotive components, particularly for Al–Si-based alloys that contain Mg and/or Cu. These alloys benefit from precipitation hardening through phases such as Mg_2Si and Al_2Cu, which can be tailored *via* post-casting heat treatments (HTs). Conventional HTs for HPDC alloys include artificial aging (T5), solution treatment followed by quenching and aging (T6), over-aging (T7), and annealing.[4,7] Among these, the T6 treatment is widely adopted to maximize strength and ductility; however, its industrial application is increasingly questioned due to its high energy demand, which can increase the overall life-cycle impact of aluminum components by up to 30 pct, as well as its susceptibility to distortion and blistering in thin-walled or large HPDC parts.[8] Attempts to reduce solution temperature or duration, to avoid blistering, often lead to incomplete solute dissolution and limited mechanical property

ELENA MINGOTTI, LUCA GIRELLI, MARIALAURA TOCCI, and ANNALISA POLA are with the Department of Mechanical and Industrial Engineering, University of Brescia, Via Branze 38, 25123 Brescia, Italy. Contact e-mail: elena.mingotti@unibs.it RICCARDO ARCALENI and ALESSANDRO MORRI are with the Department of Industrial Engineering, University of Bologna, Viale Risorgimento 4, 40136 Bologna, Italy. LUCIA LATTANZI is with the Department of Materials and Manufacturing, School of Engineering, Jönköping University, Gjuterigatan 5, 55318 Jönköping, Sweden.

Manuscript submitted November 24, 2025; accepted January 27, 2026.

Article published online February 18, 2026

improvements, undermining the effectiveness of the treatment. As a result, growing attention has been directed toward alternative, lower-energy HT strategies such as T5 and annealing, which can offer a more favorable balance between mechanical performance, dimensional stability, and environmental impact. In this context, paint-bake cycles commonly employed in automotive surface finishing processes, typically carried out in the 150 °C to 200 °C range,[9] have emerged as a promising opportunity to combine corrosion protection and mild heat treatment in a single step, potentially eliminating the need for additional artificial aging.

Furthermore, from a sustainability perspective, the use of recycled aluminum alloys is essential, as secondary aluminum production requires only about 5 pct of the energy needed for primary production, leading to substantial reductions in CO_2 emissions and industrial waste.[10,11] However, recycled HPDC alloys typically contain higher levels of impurities, particularly iron, which promotes the formation of brittle intermetallic phases such as β-Al_5FeSi, adversely affecting ductility and fracture resistance.[12,13]

Recent studies, as comprehensively reviewed by Luo *et al.*,[14] have shown that the limitations of recycled aluminum alloys can be effectively mitigated through tailored alloy chemistry, optimized Fe/Mn ratios (~ 1), as well as innovations in production and HPDC processing routes, thereby enabling their application in structural automotive components.[15–18] For crash-relevant automotive components,[19,20] however, recycled aluminum alloys must exhibit not only adequate tensile strength and elongation but also sufficient bendability and rivetability to ensure reliable forming and joining performance. These properties are particularly critical for multi-material assemblies and are routinely evaluated in the automotive industry through standardized bending and riveting tests.[21,22] Nevertheless, most of the investigations available in the literature on recycled aluminum alloys primarily focus on compositional optimization and microstructural refinement, often relying on laboratory-scale specimens. On the contrary, the combined assessment of process–microstructure–property relationships on actual automotive HPDC components remains largely unexplored in the current literature. In light of these considerations, the present study focuses on the optimization of low-energy heat treatments for a commercially available high-pressure die-cast AlSi10MnMg alloy with high-recycled-content, employed in a real automotive structural component. Artificial aging and annealing parameters were systematically varied to identify temperature–time combinations capable of enhancing mechanical performance while minimizing energy consumption. The mechanical behavior was evaluated directly on the structural casting through tensile, bending, and riveting tests, thereby addressing key industrial requirements for load-bearing and crash-relevant automotive applications. These tests enable the assessment of formability, joinability, and energy absorption capability under conditions representative of real manufacturing and service scenarios. Furthermore, a multi-scale electron backscatter diffraction (EBSD) analysis was conducted to elucidate the microstructural mechanisms governing the observed mechanical response of the alloy under different heat treatment conditions. By integrating process optimization, component-level mechanical testing, and advanced microstructural characterization, this study aims to provide practical guidelines for the sustainable deployment of high-recycled-content aluminum alloys in automotive structural applications.

II. MATERIALS AND METHODS

A. *Analyzed Components*

The present study focuses on the characterization of a thin-walled component (average thickness of 3.8 mm and maximum dimension exceeding 1000 mm), manufactured in accordance with automotive specifications for a premium carmaker. The castings were produced *via* high-pressure die casting using an AlSi10MnMg alloy with high-recycled-content (indicatively: 75 wt pct of recycling; 25 wt pct of primary alloy). The recycled aluminum alloy was obtained by remelting scrap from end-of-life consumer products which was then crushed, meticulously separated, and remelted in a multi-chamber furnace with salt fluxes to produce secondary ingots for reuse in production. Before casting, these ingots were melted in a reverberatory furnace with the addition of up to 40 pct internal returns from foundry operations (such as runner systems and overflows), further emphasizing the material circularity and environmental advantages.[23]

The chemical composition, measured by an optical emission spectrometer on a specimen taken from the holding furnace before the casting process, is reported in Table I.

To predict the solidification behavior of the recycled AlSi10MnMg alloy, a Scheil–Gulliver simulation was carried out using Thermo-Calc software, version 2024b, with the TCAL8: Al-Alloys v.8.2 database. The simulation was based on the average (avg.) chemical composition values reported in Table I.

After water quenching at room temperature following the extraction from the die, the component was trimmed to remove runners and overflows and then stored at room temperature prior to characterization thus better simulating the potential service conditions of untreated components and allowing for any natural aging phenomena to occur. This condition was considered as-produced (AP) in the current study.

Specimens were obtained through progressive cutting steps, including manual cutting and final metallographic sectioning under lubricated conditions.

B. *Optimization of Heat Treatment*

An as-produced sample (~ 10×10 mm^2) was prepared using standard metallographic procedures, including grinding followed by polishing to a mirror finish and examined by Leica DMI 5000M optical microscope equipped with Leica Application Suite v4.8 software for

Table I. Mean Chemical Composition of the AlSi10MnMg Alloy at High Percentage of Recycling, in Accordance with the EN AC 43500 Standard[23]

Al (Pct)	Si (Pct)	Mn (Pct)	Mg (Pct)	Cu (Pct)	Fe (Pct)	Sr (Pct)	Ti (Pct)	Other (Pct)
Bal.	10.63	0.40	0.41	0.04	0.19	0.017	0.08	0.07

Table II. Parameters of the Heat Treatments Performed on the HPDC Castings Made in High Recycled AlSi10MnMg Alloy

Designation	Temperature (°C)	Maintenance at Temperature	Heating Details
Artificial Aging	150	1, 2, 3, 4, 6, 8 h	cold sample in heated furnace
	170	1, 2, 3, 4, 6, 8 h	cold sample in heated furnace
	190	1, 2, 3, 4, 6, 8 h	cold sample in heated furnace
	210	1, 2, 3, 4, 6, 8 h	cold sample in heated furnace
	230	1, 2, 3, 4, 6, 8 h	cold sample in heated furnace
Annealing	350	1, 2, 3, 4 h	cold sample in heated furnace
	380	1, 2, 3, 4 h	cold sample in heated furnace
E-coating	163	20 min	heating rate of 7 ± 1 °C/min

image analysis and Zeiss Sigma 360 Field Emission Scanning Electron Microscope (FEG-SEM).

Brinell hardness was measured using a LTF Galileo Ergotest Comp25 apparatus with a WC ball (diameter of 2.5 mm) under a load of 613 N, with 4 indentations per sample.

To optimize heat treatments (HTs) a series of temperature–time combinations (Table II) were carried out using a Nabertherm P 330 laboratory furnace. The selected treatment reflected industrial practice and included artificial aging for strengthening, annealing to enhance ductility and energy absorption, and e-coating curing simulations, which may also induce precipitation hardening. Samples were air-cooled after treatment and ground with P600 abrasive paper to prepare for hardness testing.

Based on the hardness results, four representative post-processing conditions, in addition to the AP condition used as a reference, were selected for further characterization.

C. *EBSD Analysis*

Microstructural characterization was conducted using Scanning Electron Microscope (Tescan, Mira 4th generation, Brno, Czech Republic) coupled with Energy-Dispersive X-ray Spectroscopy (EDS, EDAX, Octane Elect) and Electron Back Scattered Diffraction (EBSD, EDAX, Hikari Plus), operated through the TEAM software. For each condition, a minimum of four EBSD maps were acquired: two low-magnification maps (500 μm field of view) to assess the aluminum matrix and two high-magnification maps (20 μm field of view) to analyze the eutectic regions.

Collected data were further analyzed using MTEX, an open-source MATLAB toolbox.[24] For the grain reconstruction, Low-Angle Grain Boundaries (LAGBs) were defined for misorientation angles between 2 and 15 deg, while High-Angle Grain Boundaries (HAGBs) were considered for angles exceeding 15 deg. Grains smaller than 10 and 0.02 μm were excluded from the analysis, respectively, on 500 and 20 μm field of view images, to reduce noise and artifacts, after which the grain structure was recalculated. Grain size was determined using the Feret diameter, while grain morphology was evaluated through the shape factor (SF).

D. *Tensile Tests*

Tensile tests were performed using an Instron 3369 testing machine with a load cell of 50 kN equipped with Bluehill software. The specimens were machined from plates obtained by sectioning the casting (in AP condition) and, subsequently, subjected to four different HTs. The geometry of the specimens followed the technical drawing shown in Figure 1. The characterization was conducted under displacement control, maintaining a constant strain rate of 1 mm/min. Three specimens were tested for each investigated condition. Furthermore, the fracture surfaces were analyzed by a Zeiss Sigma 360 FEG–SEM.

E. *Bending Tests*

The ductility of the alloy was further assessed through 3-point bending test carried out according to VDA 238-100 standard. The specimens were machined using a computer numerical control (CNC) machine under lubricated conditions. Each specimen was analyzed through its full thickness, which corresponds to that of the original casting (approximately 3.8 mm). For each alloy condition tested, a minimum of four specimens were characterized to determine the average bending angle.

The 3-point bending tests were performed using an Instron 3369 testing machine equipped with the Bluehill software. A rounded wedge penetrator with a radius of 0.4 mm was used and set at a descent speed of 20 mm/

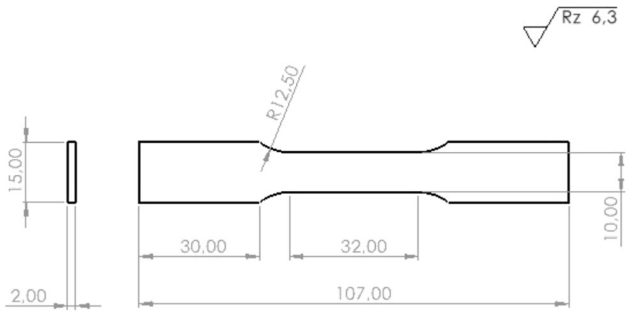

Fig. 1—Technical drawing of samples prepared for tensile test at room temperature.

min. The bending test was initiated with a 100 N preload and terminated upon reaching the yield load, identified as a 60 N drop from the maximum recorded load.

The initial angle α_{IN} generated on the sample was measured with a manual Mitutoyo goniometer. According to Eq. [1], the Bluehill software corrects the measured angle α_{IN} (corresponding to the initial specimen thickness t_{IN}) to provide the final angle α_{FIN} (corresponding to the final specimens thickness t_{FIN}), in order to convert the result to comply with the regulation that requires a thickness t_{FIN}, as well as to normalize the component with variable thickness.

$$\alpha_{FIN} = \alpha_{IN} * \sqrt{\frac{t_{IN}}{t_{FIN}}}. \qquad [1]$$

A minimum target bending angle of 50 deg at 2 mm thickness was defined. Post-test metallographic analysis were performed to investigate crack initiation and propagation mechanism.

F. *Self-Piercing Riveting Tests*

To simulate the joining of aluminum cast components *via* riveting, a self-piercing riveting (SPR) test was carried out using a Tucker® press. This test involves the penetration of a steel semi-tubular rivet through a layer of aluminum in contact with a plate made from recycled aluminum machined from the casting, both of which exhibit thickness variations of around 2 mm. The specially designed lower die prevented the rivet from completely penetrating the bottom sheet. The joint surface analysis was performed through visual inspection using a Leica DMS 300 digital measuring microscope and further analyzed with a Leica DMI 5000M optical microscope and Zeiss Sigma 360 FEG–SEM.

III. RESULTS AND DISCUSSION

A. *Scheil Simulation*

Thermodynamic simulations of this kind are essential to elucidate the influence of recycled-related impurities on the solidification path, given that intermetallic compounds can markedly affect both microstructure and mechanical properties. Therefore, a Scheil–Gulliver simulation was performed for the recycled AlSi10MnMg alloy, whose chemical composition is reported in Table I. Figure 2 shows the predicted sequence of phase formation during non-equilibrium solidification.

Solidification begins with the nucleation of primary α-Al from the liquid phase at approximately 590 °C. Then, the α-$Al_{15}(Fe, Mn)_3Si_2$ phase starts to form, promoted by the relatively high Fe and Mn contents (0.19 and 0.40 wt pct, respectively, *i.e.*, Fe/Mn ratio of 0.475). Sánchez *et al.*,[15] in their study on AlSi10MnMg alloys, reported the primary solidification of the α-$Al_{15}(Fe, Mn)_3Si_2$ phase prior to α-Al; however, this difference can be attributed to the alloy chemistry, as the composition investigated in the present work contains a lower Mn content (0.40 wt pct) compared to the alloy investigated by Sanchez *et al.*, containing 0.63 wt pct of Mn (*i.e.*, Fe/Mn of 0.19), despite a similar Fe level (0.19 *vs* 0.12 wt pct). After that, the solidification sequence continues with the formation of the eutectic constituent at around 573 °C, marking a sharp change in the solid fraction evolution. As solidification progresses, small amounts of the β-Al_5FeSi phase and π-$Al_8FeMg_3Si_6$ phase form. At later stages, the Mg_2Si intermetallic precipitates, followed by the formation of secondary α-$Al_{15}(Fe, Mn)_3Si_2$.

B. *Microstructure and Hardness of the As-produced Alloy*

The microstructural analysis of the high-recycled-content AlSi10MnMg alloy under as-produced (AP) condition showed the typical structure characterized by α-Al dendrites surrounded by the Al–Si eutectic (Figure 3). In the region close to the die wall (exhibiting maximum cooling rates[25]), named skin layer (Figure 3(a)), the dendrites are finer, while larger α-Al dendrites were observed from approximately 200 μm from the mold wall (Figure 3(a)). As known, variation in microstructure is attributed to the differing cooling rates.[26]

Externally solidified crystals (ESCs) can also be observed, *i.e.*, larger α-Al dendrites that typically form along the shot sleeve wall and near the piston tip, and subsequently are dragged by the liquid metal during the injection phase.[27] In Figure 3(b), the microstructure of the core region of the recycled AlSi10MnMg part produced *via* HPDC alloy is shown. This comprises mainly α-Al dendrites and ECSs surrounded by the eutectic region, which is made of fine slightly modified eutectic Si particles, surrounded by eutectic Al (Figure 3(c)).

The high-recycled AlSi10MnMg alloy contains additional alloying elements, mainly Fe, Mn, and Mg (Table I), which promote the development of various intermetallic phases (Figure 3(b)). In fact, in the microstructure, various intermetallic phases can be observed (Figure 3(b)), including Mg_2Si and several Fe-based compounds, as also predicted by the Scheil–Gulliver simulation performed using Thermo--Calc, such as α-$Al_{15}(Fe, Mn)_3Si_2$, β-Al_5FeSi, and π-$Al_8FeMg_3Si_6$, which may incorporate Mn and/or Mg depending on the specific alloy chemistry. The type, morphology, and size of these intermetallic compounds

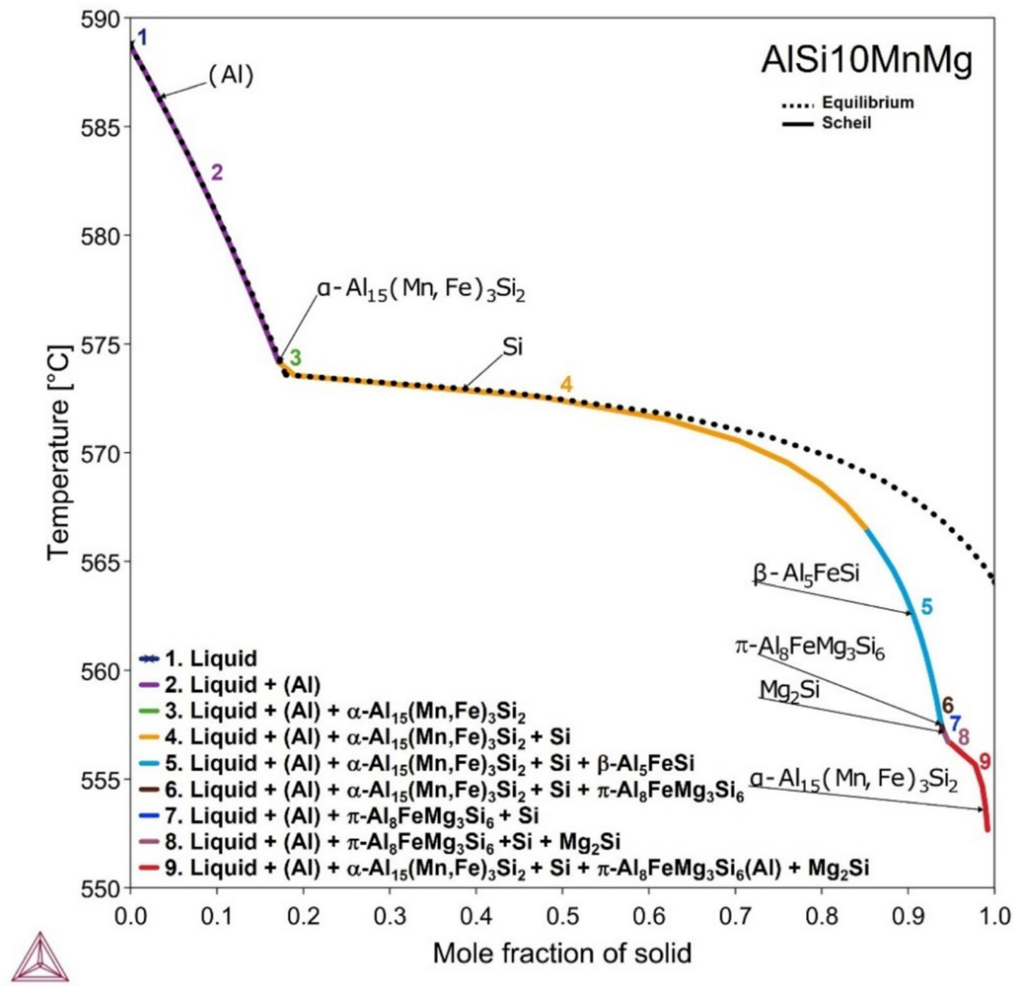

Fig. 2—Equilibrium and Scheil curves for the AlSi10MnMg high recycled alloy.

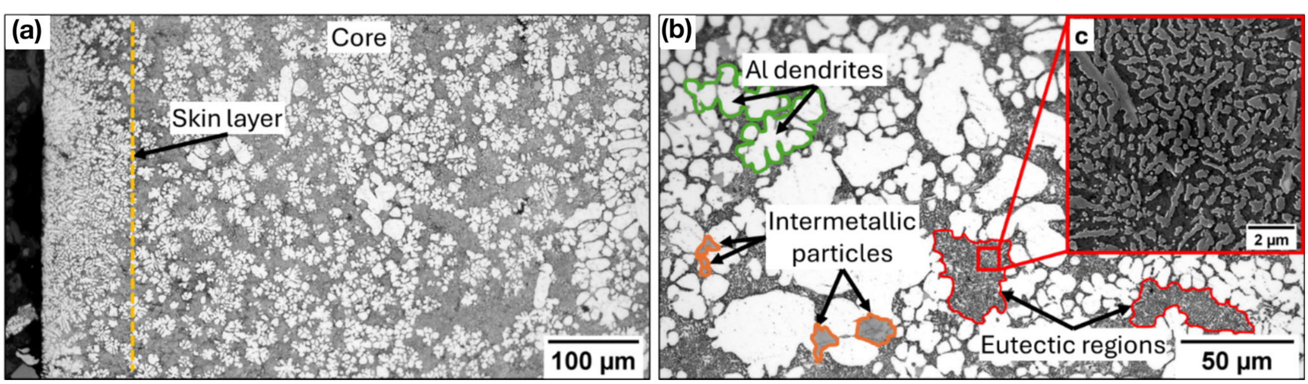

Fig. 3—Micrographs of the studied alloy in AP condition: (*a*) Low-magnification of the peripheral layer, (*b*) Magnification of the core region, and (*c*) High-magnification SEM image of the eutectic region.

are strongly influenced by multiple factors, primarily the chemical composition and cooling rates during solidification, as reported in Reference 15. Figure 4 exemplifies these microstructural features. The elemental distribution maps of Al, Si, Mn, and Fe (Figures 4(b through e)) support the identification of the secondary interdendritic α-$Al_{15}(Fe, Mn)_3Si_2$ phase, which often appears in a characteristic Chinese-script morphology, whereas the primary α-$Al_{15}(Fe, Mn)_3Si_2$ particles are generally larger and with a polygonal shape. In addition, small, dark-contrast particles are visible in the Back Scattered Electron (BSE) micrograph (Figure 4(a)), consistent with phases of low average atomic number. Their composition is confirmed as Mg_2Si by the EDS map

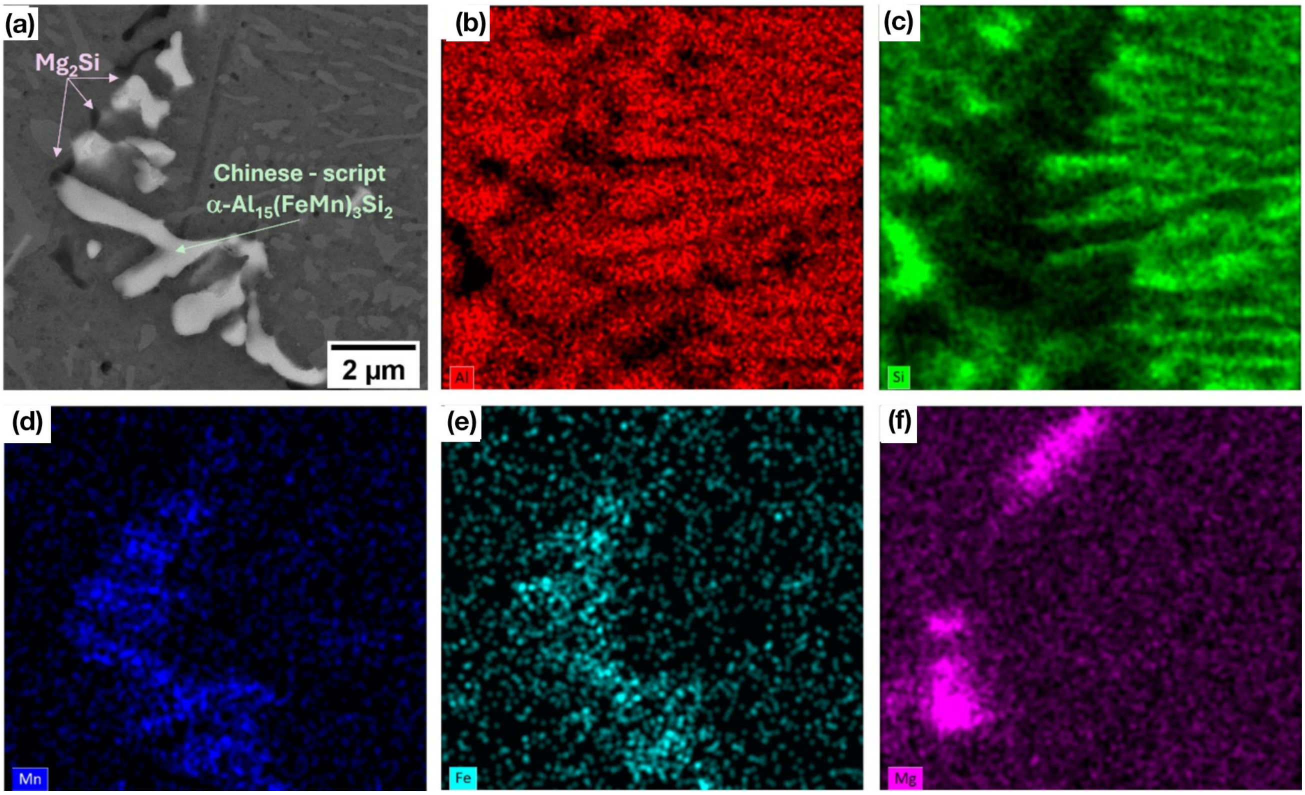

Fig. 4—SEM–BSE micrograph (*a*) and corresponding EDS elemental maps (*b* through *f*) of some intermetallic compounds observed in the microstructure of the recycled AlSi10MnMg alloy in the AP condition. Elemental distribution maps: (b) Al, (c) Si, (d) Mn, (e) Fe, and (f) Mg.

(Figures 4(c and f)). Intermetallic particles tend to be more brittle than the aluminum matrix, limiting the material ability to deform plastically under load; this results in reduced ductility, which in turn lowers the material ability to absorb energy before fracturing.

The AP sample showed a hardness of 88 ± 1 HBW 2.5/62.5. This result is quite high for an AlSi10MnMg alloy in as-cast state considering that in the literature values of about 77 ± 3 HBW 2.5/62.5 are common.[28] This can be the consequence of the high cooling rate of the casting due to water cooling after extraction from the die and the following natural aging.

C. *Hardness of Aging Conditions*

The aging curves in terms of Brinell hardness obtained (after aging treatments listed in Table II) are reported in Figure 5. An exposure of 0 minutes corresponds to the as-produced condition. The maximum st. dev. recorded is equal to 1 HBW 2.5/62.5, and therefore not appreciable in the plotted data.

Lower aging temperatures tested in this work (specifically: 150 °C, 170 °C, and 190 °C) generally showed the increasing trend in hardness with increasing treatment time, reaching a peak at 3 to 4 hours of 106, 114, and 112 HBW 2.5/62.5, respectively. This behavior is attributed to the progressive precipitation of strengthening phases Mg_2Si phases during aging treatments.[29] For these lower temperatures, the hardness curves exhibit a plateau from approximately the fourth hour onward, with average values of 104, 112 and 109 HBW 2.5/62.5, respectively. This plateau indicates the onset of over-aging, when precipitates grow and coalesce, reducing their strengthening effect. At 150 °C, slower precipitate growth delays this process, so no distinct plateau is observed.[30,31]

At higher aging temperatures, specifically 210 °C and 230 °C, the over-aging phenomenon manifests earlier, becoming evident already after 2 hours from the beginning of the treatment. Additionally, samples aged at these temperatures reach lower peak hardness, 108 and 109 HBW 2.5/62.5 (avg.), respectively. This decrease is attributed to the accelerated kinetics of precipitate coarsening, driven by faster growth and coalescence, and by the reduced nucleation of new particles, which ultimately leads to a loss of mechanical strength.[8]

D. *Hardness of Annealing Conditions*

The hardness evolution of the samples after annealing treatments is reported in Figure 6.

An exposure of 0 minutes corresponds to AP condition. The maximum st. dev. is equal to 0.6 HBW 2.5/62.5, thus not noticeable in the chart.

The annealing treatments performed at both 350 °C and 380 °C did not result in any increase in hardness compared to the AP condition. At these high temperatures, in fact, hardness tends to decrease with increasing treatment time. This phenomenon is associated with

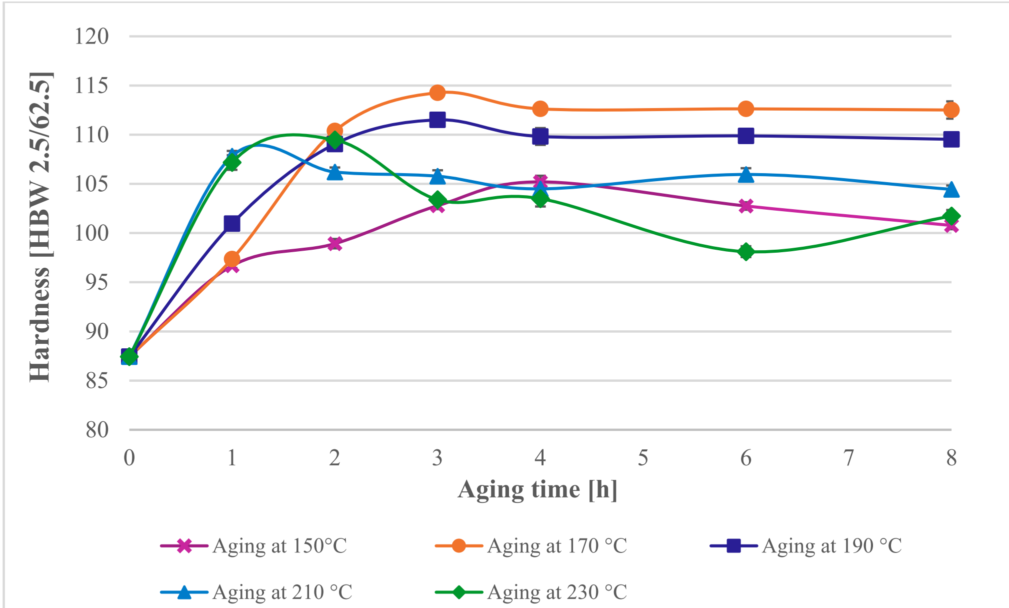

Fig. 5—Results of Brinell hardness tests of HPDC AlSi10MnMg samples after aging treatments performed at 150 °C, 170 °C, 190 °C, 210 °C, and 230 °C for a duration of 1, 2, 3, 4, 6, 8 h. An exposure of 0 minutes corresponds to the AP condition.

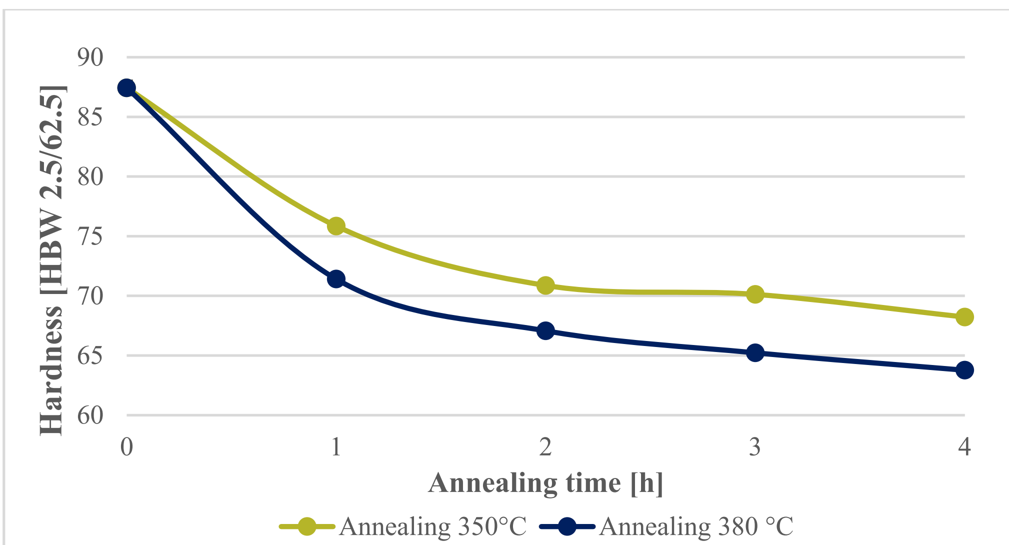

Fig. 6—Results of Brinell hardness tests of HPDC AlSi10MnMg samples after annealing treatments performed at 350 °C and 380 °C for duration of 1, 2, 3, 4 h. An exposure of 0 min corresponds to AP condition.

microstructural coarsening and the evolution or partial dissolution of secondary particles like Si and Mg_2Si, which ultimately lowers the material strength,[32] as illustrated in the subsequent chapter.

E. *E-coating*

The values obtained from the post-processing e-coating treatment are summarized and compared to the as-produced condition in Table III.

Table III. Results of Brinell Hardness Tests of HPDC AlSi10MnMg Samples in AP Condition and After E-coating

	[HBW 2.5/62.5]	
	Avg.	St. Dev.
As-produced	87.4	0.6
E-coating (163 °C)	97.4	0.1

The results indicate an increase in hardness of about 11.4 pct after the e-coating simulation at 163 °C, indicating that the post-processing treatment also enhance the mechanical properties by acting as an aging treatment, since the castings are exposed to temperatures comparable to those used in conventional artificial aging.

F. *Selection of the Conditions for Further Characterization*

Based on the hardness results, the most promising conditions from an industrial standpoint were identified to exploit the material mechanical properties for specific application requirements. The following conditions were further investigated through tensile, bending, and self-piercing riveting tests:

(1) As-produced (AP) condition, used as a reference.
(2) E-coating simulation (EC) at 163 °C-20 min, selected to evaluate the effect of a typical automotive post-processing treatment on the mechanical properties of the material.
(3) Artificial aging (AA) performed at 170 °C-3 h, chosen as it represents the temperature-time combination to achieve peak hardness (Figure 5).
(4) Over-aging (OA) at 210 °C-3 h, considered as it results in a decrease in hardness after the peak (Figure 5) but is expected to provide improved microstructural stability and long-term performance.
(5) Annealing (AN) at 380 °C-3 h, chosen to reduce hardness to a minimum, as demonstrated in Figure 6, but expected to enhance the material ductility.

G. *Microstructure Analysis Heat Treatments*

In Figure 7, micrographs of samples after the selected heat treatments are shown. As expected, no significant growth of α-Al dendrites was observed, indicating that the simulation of the post-processing and the two selected aging treatments do not cause appreciable microstructural variations at these magnifications (Figures 7(a, c, e, g, and i)). The SEM micrographs (Figures 7(b, d, f, h, and j)) clearly show the presence of eutectic Si particles, whose morphology and spatial distribution have been significantly altered by the heat treatment. In the AP condition (Figure 7(b)), the eutectic Si phase forms a uniformly distributed, interconnected network within the matrix. The average size remains largely unchanged in the EC and AA conditions (Figures 7(d and f)), suggesting that these HTs do not induce significant coarsening. Notably, in the AA condition, the eutectic Si network appears finer and more elongated, indicative of morphological rearrangement. The OA condition (Figure 7(h)) exhibits partial coarsening and the initial stages of spheroidization, reinforcing the role of temperature as a key factor driving morphological evolution of the eutectic Si phase. The most substantial transformation is observed in the AN condition (Figure 7(j)), where the Si particles undergo extensive spheroidization and coarsening, resulting in discrete, rounded morphologies with significantly reduced interconnectivity. These microstructural changes underscore the high sensitivity of the eutectic Si phase to thermal exposure and suggest a strong correlation between heat treatment parameters and the resulting mechanical properties of the alloy.

Figure 8 shows representative EBSD grain maps of the AlSi10MnMg alloy in the AP, AA, and AN conditions. Both aluminum and eutectic Si grains were considered in the analysis. Figures 8(a through c) display low-magnification images that highlight the crystallographic orientation, morphology, and spatial distribution of α-Al dendrites and randomly dispersed externally solidified crystals (ESCs).[33] Figures 8(d through f), on the other hand, provide higher magnification views of the microstructure focused on the eutectic regions, enabling a more detailed assessment of eutectic aluminum and silicon particles. Grain boundaries are delineated in black, while red lines indicate the presence of sub-grains. A threshold misorientation angle of 15 deg was applied to separate low-angle and high-angle grain boundaries (LAGBs and HAGBs), as well as to distinguish individual grains and sub-grains. Additionally, Figure 8 shows that the Kernel Average Misorientation (KAM) maps highlight differences in local plastic deformation across the three conditions. In the AP and AA conditions, numerous localized zones of high misorientation, particularly adjacent to eutectic regions, are observed. These regions are likely indicative of dislocation accumulation arising from the casting process, especially in rapidly cooled thin-wall components characterized by high residual stresses. The AA treatment does not appear sufficient to significantly relieve these residual stresses. In contrast, these red zones in KAM maps of Figures 8(a and b) become progressively less pronounced in the AN condition (KAM map Figure 8(c)), suggesting that partial recovery and dislocation rearrangement have occurred because of thermal exposure at 380 °C for 3 hours. Nevertheless, the α-Al matrix in the AN sample appears more uniformly red in the KAM map, indicating a softer microstructure that is more susceptible to work hardening during metallographic preparation. Conversely, the dendrites in the AA condition appear whiter, reflecting less surface induced plastic deformation, which is consistent with the increased hardness achieved through artificial aging.

This multi-scale EBSD analysis enabled an in-depth evaluation of the recycled alloy microstructure across different heat treatments. The investigation also included quantitative analysis of the size and shape factor distributions of both α-Al and eutectic Si particles (see Figure 9), as well as grain orientation and anisotropy evaluation via pole figures (see Figure 10). These microstructural characteristics are of particular

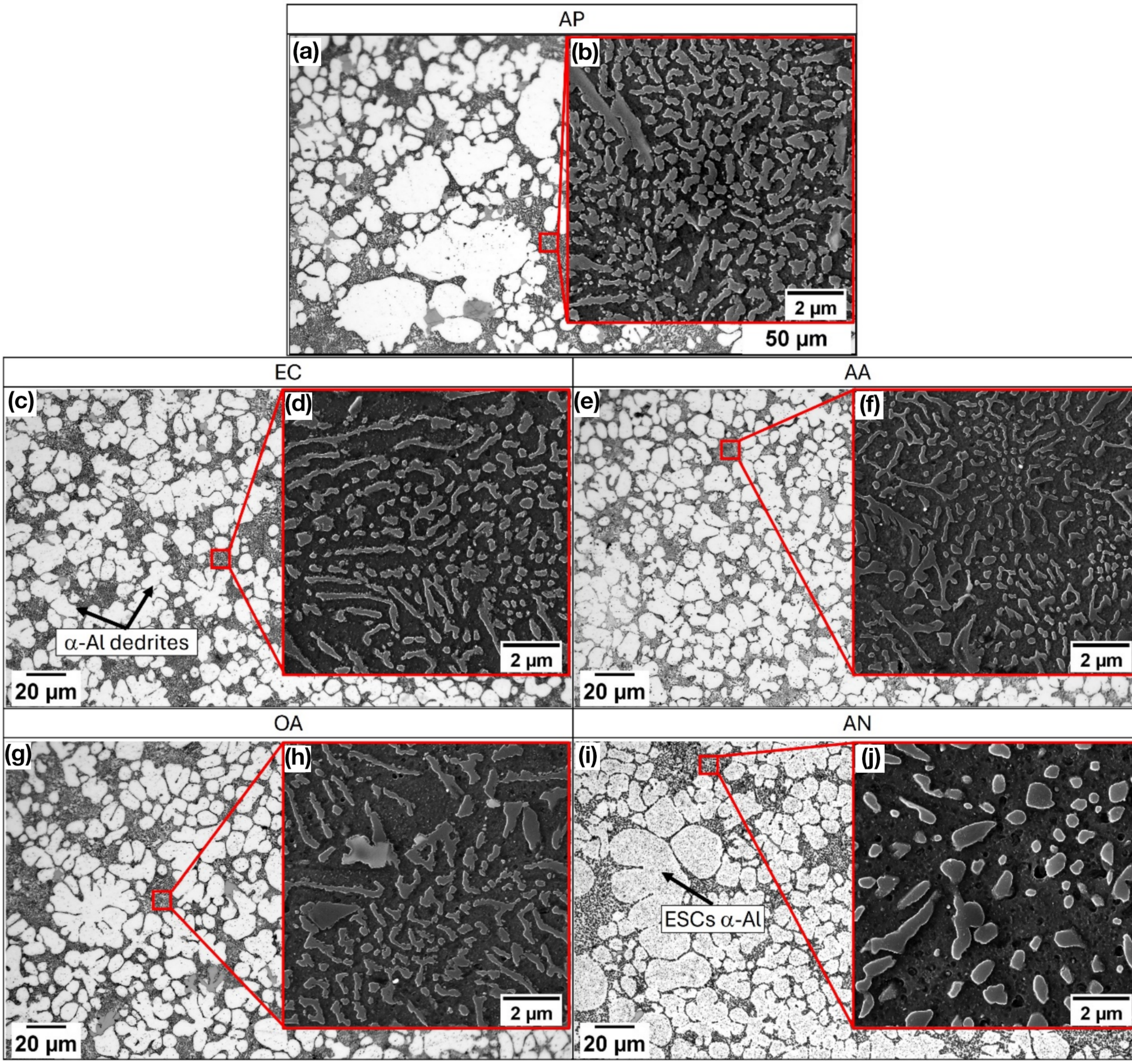

Fig. 7—OM micrographs (*a*, *c*, *e*, *g*, *i*) with a high magnification focus in Secondary Electron (SE) SEM images (*b*, *d*, *f*, *h*, *j*) of the eutectic region for a recycled AlSi10MnMg alloy in the: (a, b) AP; (c, d) EC; (e, f) AA; (g, h) OA; and (i, j) AN conditions.

importance, as they play a key role in determining the alloy mechanical and physical performance, as previously reported by References 34 and 35.

The AP, EC, AA, and OA conditions exhibit fine microstructures, with average grain sizes of approximately 30 μm for α-Al and 0.6 μm for eutectic Si. In all cases, occasional grains exceeding 100 μm were observed, indicating the presence of large externally solidified crystals (ESCs). These observations agree with the findings of Jiao *et al*.,[36] who reported similar features in HPDC primary AlSi10MnMg alloys.

The eutectic Si phase in the AN condition appears slightly coarser, with an average size of approximately 0.8 μm. However, this mean value mainly serves to highlight the overall trend and should be interpreted with caution, as the distributions shown in Figure 9(c) reveal a large number of fine Si particles that reduce the average value. Moreover, elongated Si particles with relatively large Feret diameters are still present in the AP, EC, AA, and OA conditions, which can mask the actual extent of coarsening when relying solely on average size.

To better capture the combined effects of coarsening and spheroidization, the shape factor (SF) is also considered. As shown in Figure 7, AN promotes partial spheroidization of eutectic Si, reflected by a lower SF average value of 1.46 compared with 1.55 in the AP condition. These differences are primarily attributed to the influence of thermal exposure, which facilitates coarsening and partial spheroidization of eutectic Si particles, especially in thin-walled HPDC components.[37] This effect becomes increasingly evident with

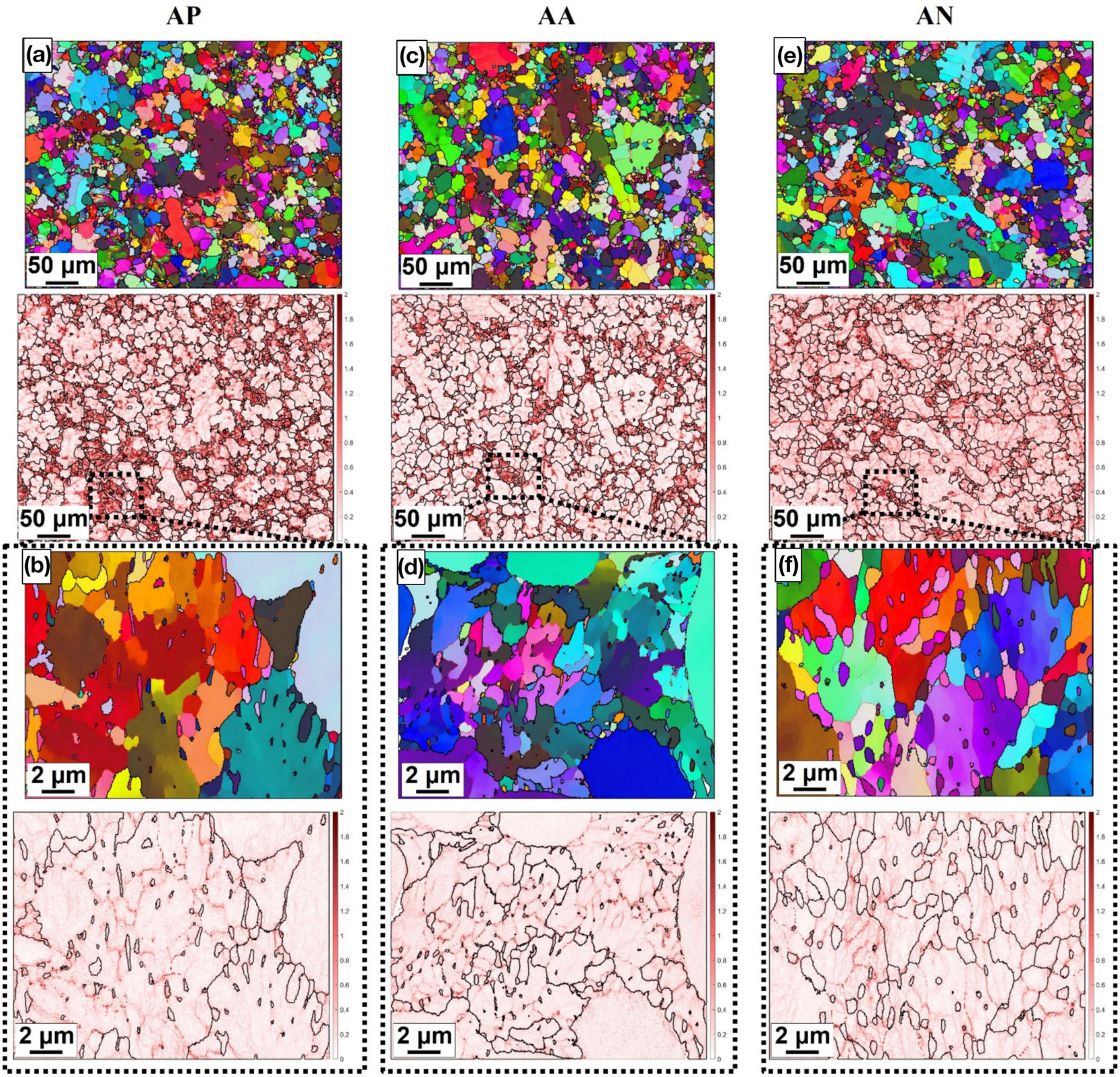

Fig. 8—EBSD grain maps and Kernel Average Misorientation (KAM) maps at low and high magnification of the AlSi10MnMg HPDC alloy in the following conditions: (*a*, *b*) AP, (*c*, *d*) AA, and (*e*, *f*) AN.

higher temperatures and longer durations of heat treatment, as is the case for the AN condition. A slight increase in particle roundness is also noted in α-Al grains for artificial aging (AA and OA) and annealing (AN) conditions compared with the AP.

Moreover, thermal treatments enhance the homogeneity of grain misorientation, confirming the activation of partial recovery mechanisms. As shown in Figure 10, the AN condition exhibits a weaker and more randomized crystallographic texture when compared to AP and AA. In the AP condition, a pronounced texture is evident, reflecting the directional solidification imposed during die casting. Upon heat treatment, particularly AN, this preferential orientation gradually fades due to partial recovery and increased grain boundary mobility, resulting in a more isotropic microstructure.

H. *Tensile Test*

In Figure 11 the mean values and the corresponding standard deviations of yield strength (YS), ultimate tensile strength (UTS) and elongation (EL) for the studied alloy after the different heat treatments are reported.

The results showed that the tensile strength of the material varies significantly with the temperature of the treatments.

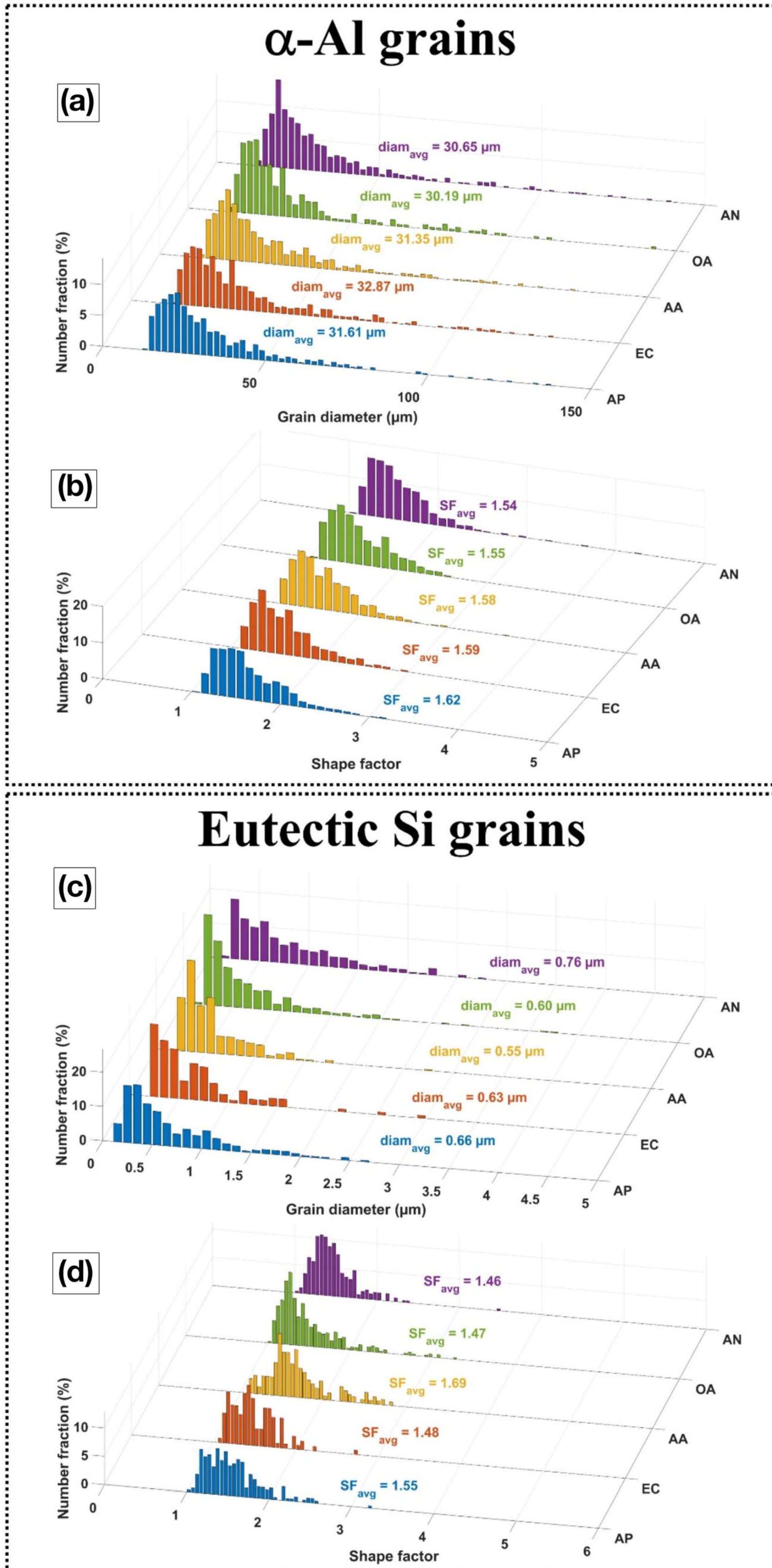

Fig. 9—α-Al and eutectic Si grains distribution of the diameter and shape factor of the recycled AlSi10MnMg in the investigated conditions: AP, EC, AA, OA, and AN.

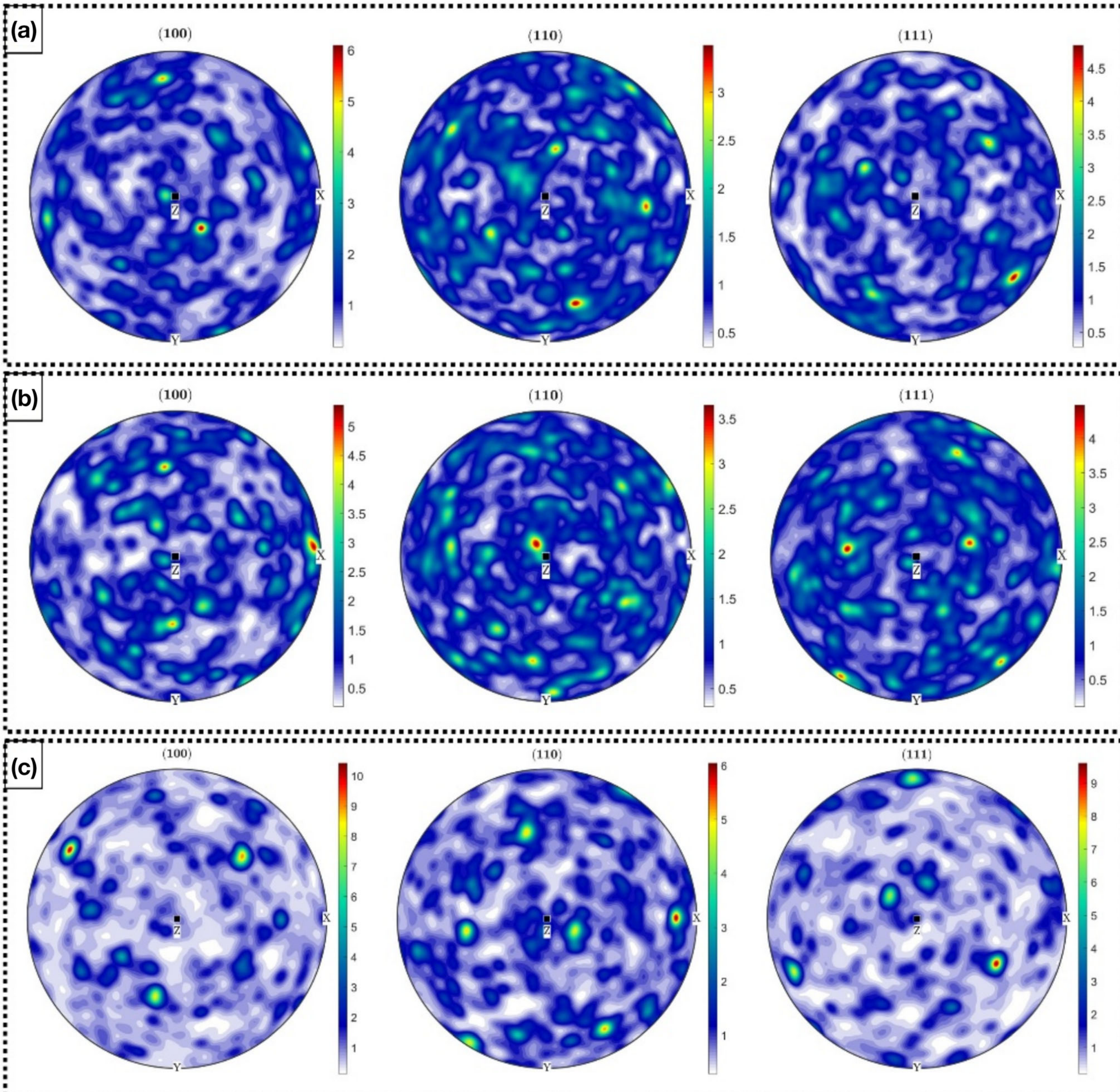

Fig. 10—(100), (110), and (111) pole figures of recycled AlSi10MnMg HPDC alloy in the following conditions: (*a*) AP, (*b*) AA, and (*c*) AN.

The AA treatment showed the most significant increase in UTS (+ 11.3 pct compared to AP condition), while the OA sample exhibited only a minor change (+ 1.0 pct). Conversely, EC let to a slight decrease in tensile strength (– 2.6 pct), which is essentially comparable to the AP condition when considering the standard deviations. The most drastic decrease was observed after AN (– 36.9 pct). Comparing the UTS of AN with that of AA, a difference of 149 MPa (avg.) can be appreciated (– 43.3 pct).

Elongation at break follows an opposite trend to tensile strength, with the AN treatment yielding the highest ductility (EL = 15.5 pct), roughly three times that of AA and a + 103.9 pct increase compared to the AP. A similar improvement in ductility after annealing has been reported by Jarco,[38] who observed a maximum increase following a soft annealing treatment at 370 °C for 8 hours. The EC and both the aging treatments resulted in a significant decrease in elongation with a variation, in comparison with the AP condition, of – 13.2, – 23.7, and – 27.6 pct, respectively.

Regarding yield strength, the aging treatments resulted in an increase in YS, with the AA treatment showing the most significant increase (+ 42.3 pct) compared to the AP condition. EC treatment leads to a

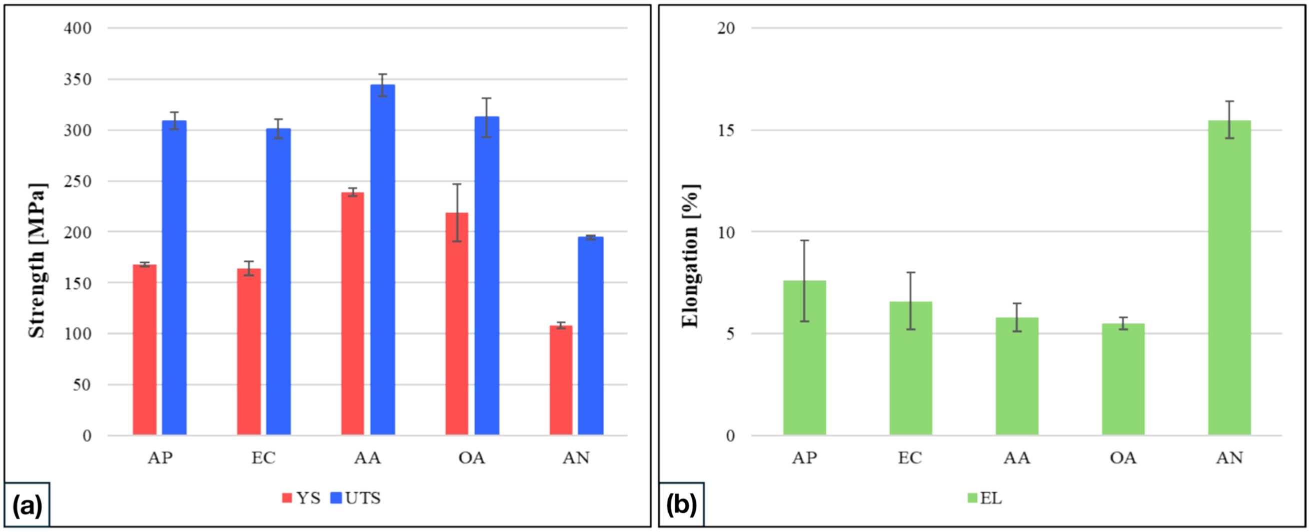

Fig. 11—Results of (*a*) YS and UTS and (*b*) EL for the high recycled AlSi10MnMg samples as a function of the heat treatments.

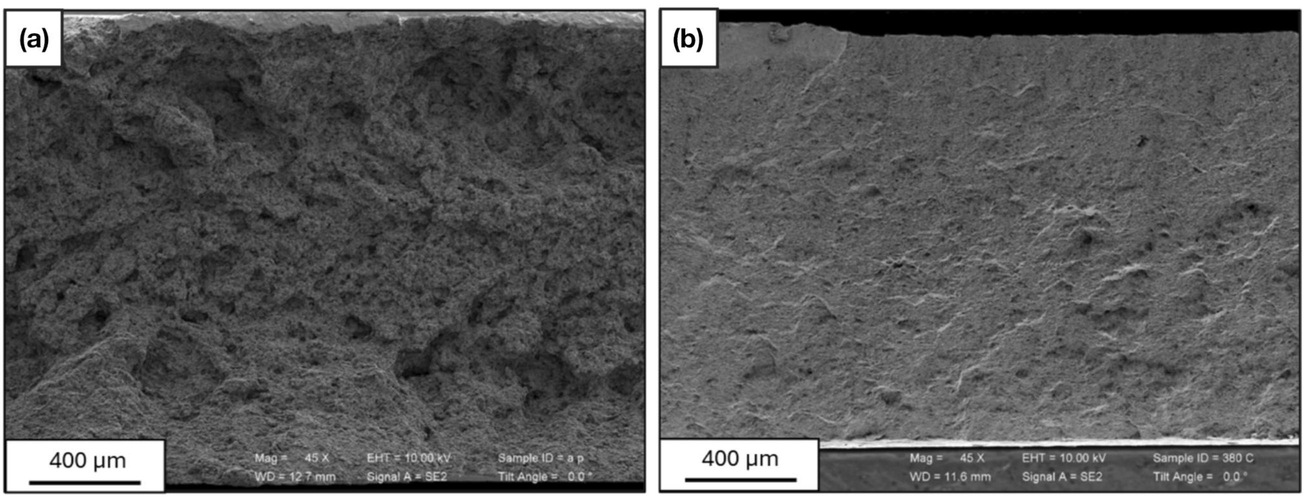

Fig. 12—Surface fracture of HPDC AlSi10MnMg samples under (*a*) AP and (*b*) AN conditions.

light decrease in YS, with a variation of − 2.4 pct; the greatest reduction in strength was observed with AN treatment (− 35.7 pct).

These tensile test results are fully consistent with, and in some cases superior to, those reported in studies available in literature[33,37,39,40] on as-cast and heat--treated (aging and annealing) Al–Si alloys manufactured by HPDC.

I. *Fractographic Characterization*

SEM–SE fractography after tensile testing (Figure 12) shows that only the AP and AN conditions exhibit a distinct fracture morphology, as the intermediate HTs (EC, AA, OA) display fracture features similar to AP, consistent with the comparable microstructure observed in Figure 7.

The fracture surface of the AP sample (Figure 12(a)) shows a highly irregular and rough morphology, characterized by numerous cavities. In contrast, the fractured AN sample (Figure 12(b)) appears significantly smoother, with a flatter and more homogeneous morphology. This marked reduction in surface roughness and the more cohesive appearance is consistent with the spheroidization and coarsening of eutectic Si particles reported in Figure 7(j), which reduces stress concentrations and facilitates plastic deformation of the α-Al matrix. These combined effects explain a transition towards a more ductile fracture mechanism, likely associated with the redistribution of internal stress and a softening of the material induced by thermal exposure.[4]

The fracture surface analysis of the AP, EC, AA and OA samples revealed a heterogeneous morphology, as noticeable at higher magnification (Figure 13), characterized by varying degrees of ductility depending on the observed area. The microstructure resulting from these conditions contributes to higher mechanical strength

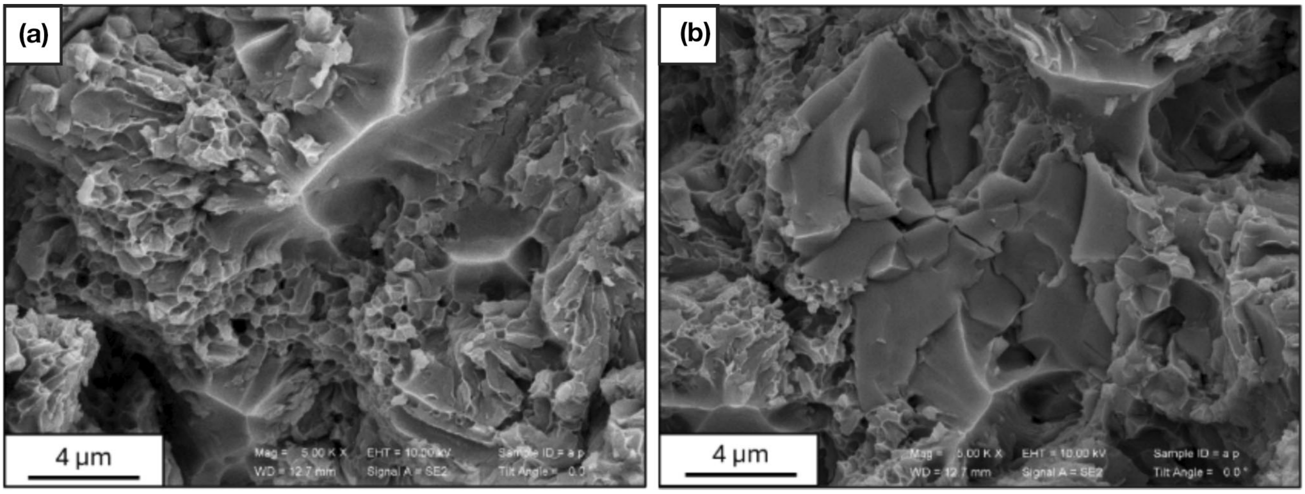

Fig. 13—Heterogeneous microstructure of HPDC AlSi10MnMg samples in (*a*) AP and (*b*) EC conditions.

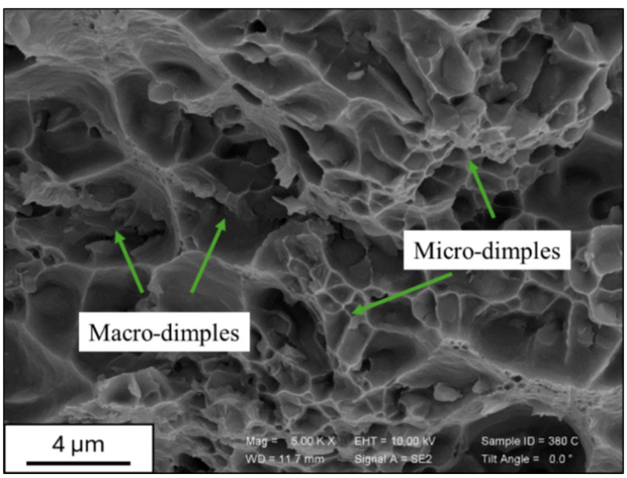

Fig. 14—Microstructure of HPDC AlSi10MnMg samples after the AN treatment.

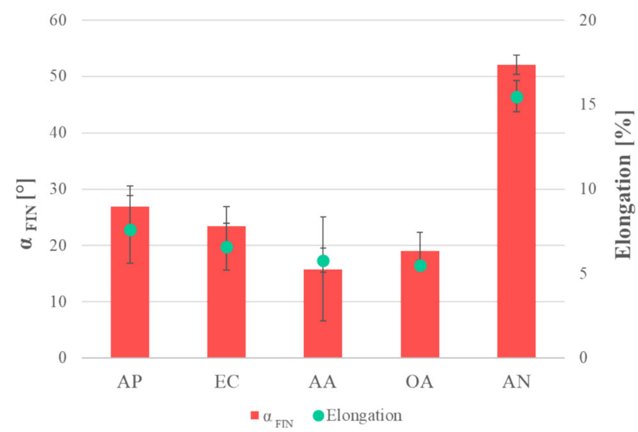

Fig. 15—Results of α_{FIN} after the bending tests of HPDC high-recycled AlSi10MnMg samples as a function of the heat treatments in comparison with the elongation measured during the tensile test.

compared to the AN condition, but at the expense of ductility, as already shown in Figure 11. As observed under SEM (Figure 13(a)), the finer and more interconnected eutectic Si morphology in the AP condition promotes the formation of localized deformation zones, where the matrix experiences only limited plastic strain. Furthermore, the KAM maps (Figure 8) indicate that these regions coincide with areas of high dislocation density and residual stress, further limiting plastic deformation and promoting crack initiation around hard particles. The presence of tear ridges in the AP condition (Figure 13(a)) indicates localized plastic deformation of the Al matrix prior to final failure, associated with crack blunting and interaction with hard particles that locally hinder crack propagation.[41]

Crack propagation can occur through multiple microstructural features. In particular, α-Fe phases were frequently observed on the fracture surface of recycled aluminum alloys, consistent with previous reports,[37] indicating that the fracture propagates along these particles as well as along the Al–Si interface (Figure 13(b)). The brittleness of eutectic Si particles is linked to their tendency to cleave along specific crystallographic planes, resulting in sharp, faceted fracture surfaces. Acting as rigid inclusions with limited deformability, these particles hinder plastic flow in the surrounding Al matrix leading to localized stress concentrations that promote crack initiation and accelerate crack propagation.[33]

On the contrary, AN-treated samples (Figure 14) exhibit a fully ductile fracture with relatively uniform, deep dimples. In particular, the fracture surface shows large, rounded macro-dimples around coarsened Si particles, containing finer micro-dimples associated with smaller Si particles or impurities, consistent with SEM and EBSD observations. Spheroidization of Si during AN (Figure 7) lowers stress concentration, promoting local void nucleation, growth, and coalescence. This morphology reflects increased toughness, as the ductile fracture mechanism enables greater energy absorption before failure, as highlighted by Figure 11.

Overall, the combination of SEM, EBSD, and KAM observations enables a coherent interpretation of the mechanical behavior: treatments that maintain a fine interconnected Si network and a high density of strengthening precipitates enhance strength but reduce ductility, whereas those promoting Si spheroidization and precipitate coarsening (AN) improve ductility at the cost of tensile strength, as reflected in the UTS and elongation values reported in Figure 11.

J. *Bending Test*

The results of the avg. bending angles (Eq. [1]) for each HT are reported in Figure 15.

In the AP condition, the material exhibited a bending angle below the optimal threshold for automotive structural components (> 50 deg). The EC (23.5 deg), AA (15.8 deg), and OA (19.1 deg) treatments further reduced the bending angle, indicating decreased ductility compared to the AP condition (see Section III–G).

Only the AN treatment allowed the material to exceed the industrial benchmark, reaching 52.1 deg, consistent with the enhanced ductility observed in tensile tests (Figure 11). The improved bending performance indicates that AN treatment effectively increases the material capacity to deform under load, making it more suitable for applications where ductility is essential.

Images of tested samples are shown on Figure 16. During the bending test, the sample is subjected to a bending moment that induces deflection, leading to varying stress distributions across the cross-section: one surface experiences tensile stress, while the opposite one is under compression. Microstructural imperfections such as porosity, inclusions, microscopic cavities, or internal defects can act as stress concentrators and facilitate crack initiation. Once initiated, cracks propagated along the path of least resistance, guided by the microstructural configuration and the distribution of phases,[42] including intermetallic compound or other secondary phases, whose hardness and bonding with the aluminum matrix influenced the crack trajectory. However, it should be emphasized that the porosity level was consistently below 0.05 pct in all conditions, indicating that porosity did not significantly influence the differences in treatment performance.

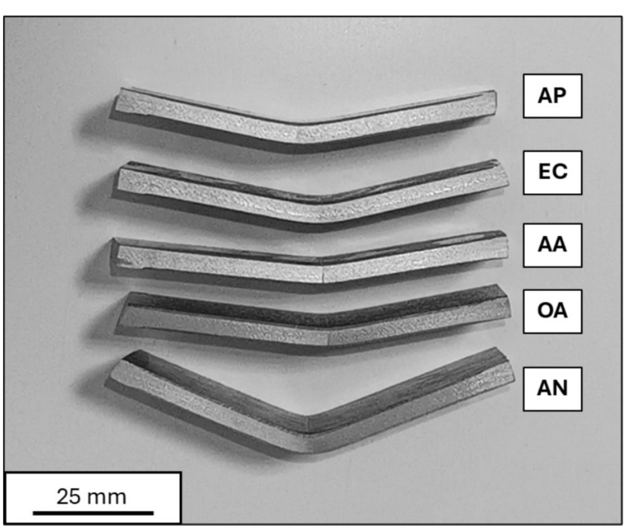

Fig. 16—Samples after the three-point bending test in AP, EC, AA, OA, and AN conditions.

The fracture shown in Figure 17, taken as a representative example of the AP, EC, AA, and OA conditions, can be explained by the microstructural observations reported in Figures 7, 8, 9, and 10. In these HT conditions, the eutectic Si phase retains a fine, interconnected morphology (Figures 7(a through h)), which, together with the presence of α-Fe intermetallic compounds, creates preferential paths for crack initiation and propagation along dendrite boundaries. EBSD and KAM maps (Figures 8(a and b)) further highlight localized zones of high misorientation and dislocation density adjacent to eutectic regions, consistent with residual stresses that promote a less ductile crack growth under bending. These features explain the reduced bending angles observed for these conditions.

In contrast, after AN treatment, the eutectic Si particles undergo morphological spheroidization (Figure 7(j)) reducing stress concentrations at the Al–Si interfaces. KAM maps (Figure 8) show partial dislocation recovery and a more homogeneous and softer α-Al matrix. These microstructural changes delay crack initiation and promote ductile deformation, allowing the material to sustain larger bending angles and explaining the superior bending performance of the AN condition.

K. *Self-Pierce Riveting Test*

The effectiveness of the riveting process was evaluated through a dual approach combining visual inspection and sectional analysis (Figure 18). Both methods confirmed proper rivet perforation and joint formation without fully penetrating the lower cast AlSi10MnMg plate.

Defects and cracks were observed in the AP, EC, AA and OA treatments, with cracks clearly highlighted in red in Figure 18, whereas the AN condition showed no defects, reflecting its improved microstructure and enhanced ductility. Only the AN treatment among the five tested conditions fully meets automotive sector requirements, demonstrating high ductility during the riveting phase. This aligns with the literature,[43] which indicates that SPR joinability improves with higher elongation and lower yield strength, conditions that, in our study, are achieved with the AN treatment, as shown in Figure11.

To further elucidate the difference between the AN condition, which successfully passed the riveting test, and the AA condition, representing the most critical case due to its highest hardness (Figure 6) and UTS (Figure11), an additional microstructural investigation was conducted using FEG–SEM.

In Figure 19(a), the AN condition, and similarly the AA condition, exhibits two distinct morphological features. The II, IV regions show a clear adhesion of the AlSi10MnMg alloy to the die surface, with a finishing pattern that faithfully replicates the geometry

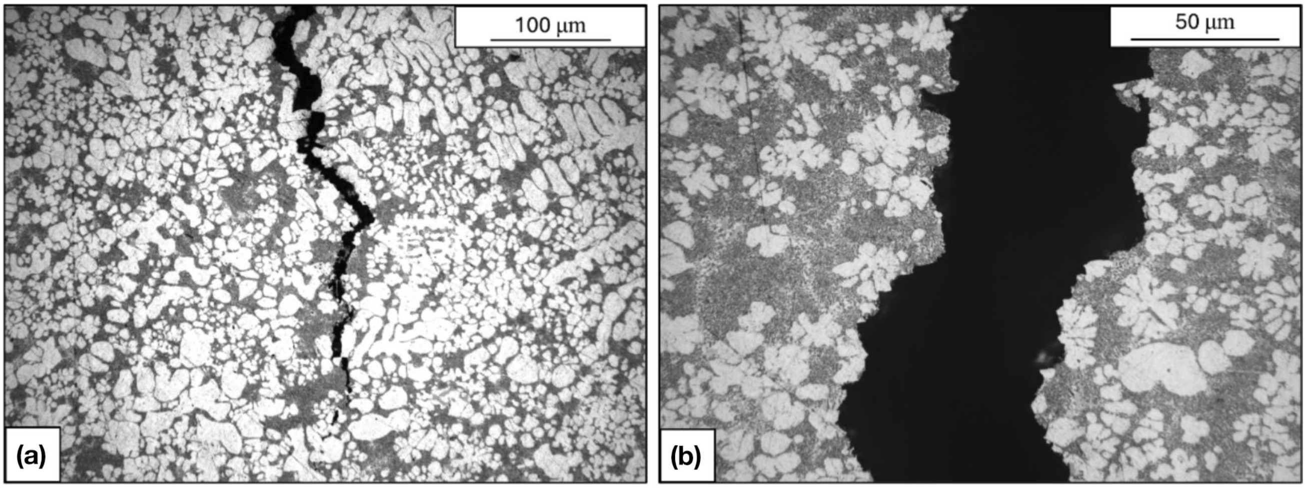

Fig. 17—Crack microstructure after the bending test of a HPDC in AlSi10MnMg samples at AP condition observed through the means of optical microscopy at low (*a*) and high (*b*) magnification.

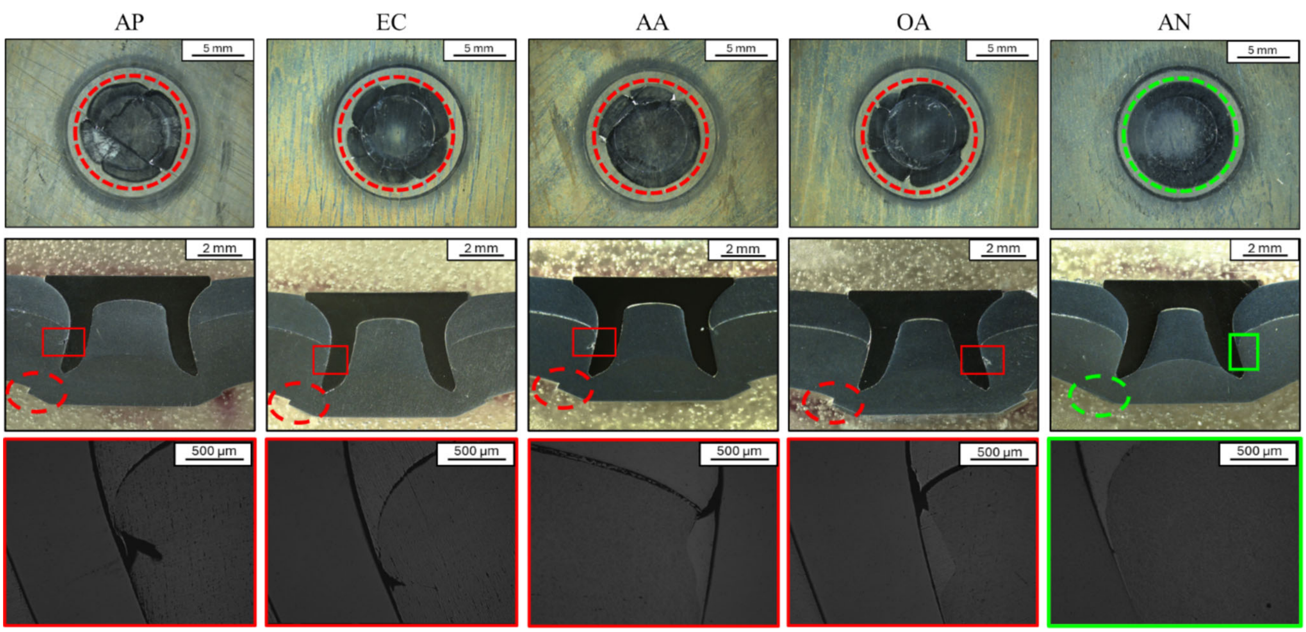

Fig. 18—Comparison between visual inspection and sectional analysis as a function of the HTs.

of the die used during the riveting test. In contrast, the I, III areas correspond to portions of the alloy that did not come into contact with the die and therefore preserve their original surface finish. A closer view of region III in Figure 19(b) reveals that the material undergoes plastic stretching without fracture, unlike the case in Figure 19(d), where the stretched material instead fails and loses continuity. The AN treatment increases the alloy ductility by promoting partial recovery of the α-Al matrix and extensive spheroidization of the eutectic Si particles (Figures 7(i) and (j) and 9), which reduces their interconnectivity and sharp edges. As a result, the material can undergo greater plastic deformation before failure and can absorb more energy during mechanical loading, while the rounded Si particles mitigate stress concentrations and improve overall deformation homogeneity.

The AA condition (Figures 19(c and d)), displays evident tearing and fracture phenomena, consistent with the defects already identified during the visual inspection in Figure 18. The purple triangle in Figure 19(d) marks the internal position of the rivet. Due to the limited elongation associated with this treatment (Figure 11), as also reported in Reference 44, microcracks can form around the rivet tail as a result of severe plastic deformation and metal flow during riveting. During this process, the bottom sheet, compressed onto the top sheet, fills the die,[45] exposing its lower surface to tangential tensile stresses. When these stresses exceed the permissible deformation of the material, radial cracks

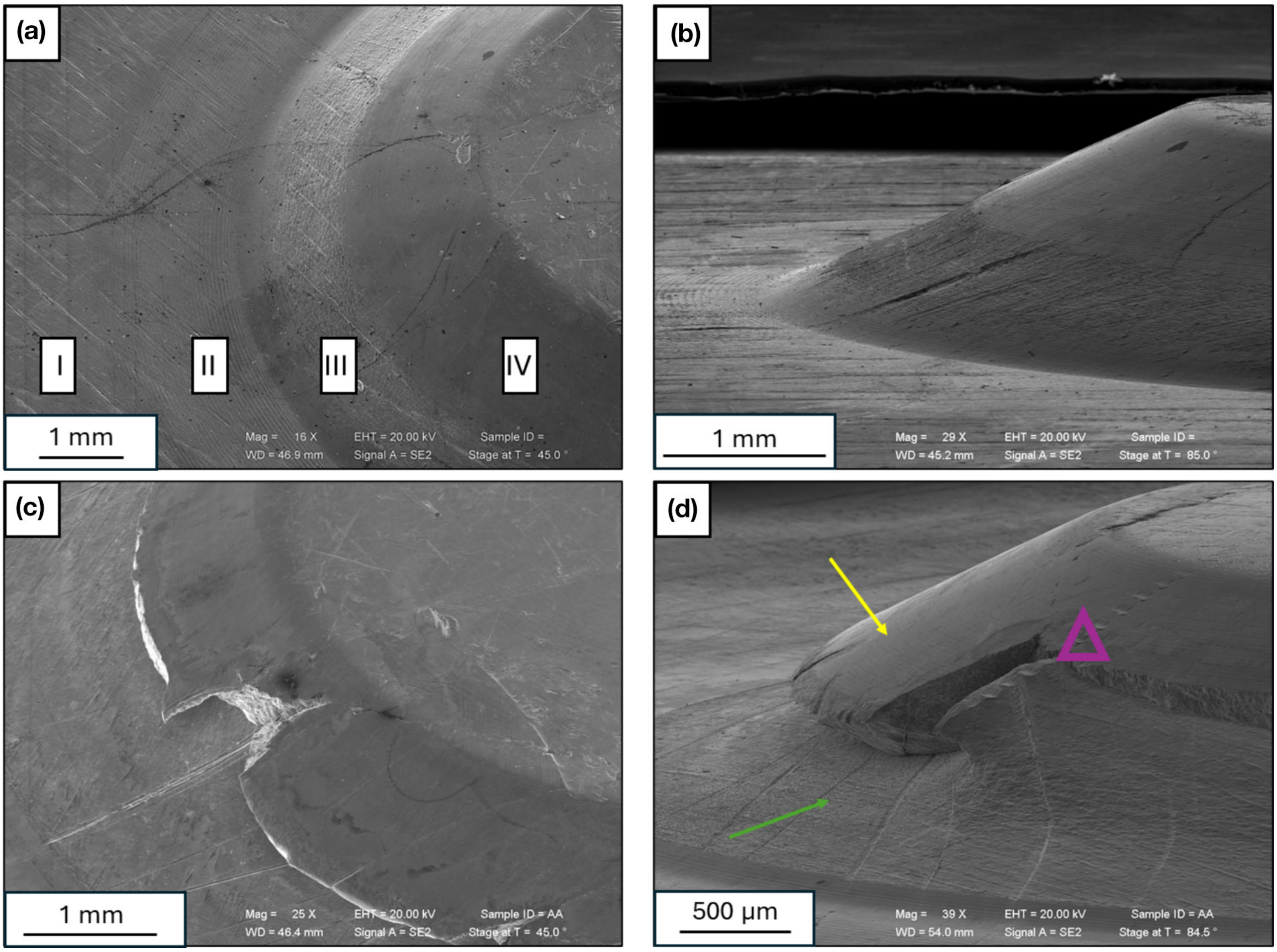

Fig. 19—FEG–SEM micrographs of the AlSi10MnMg alloy after riveting tests under (*a*, *b*) AN and (*c*, *d*) AA conditions.

develop,[46,47] as also visible in Figure 18. Furthermore, once the rivet has displaced and lifted the AlSi10MnMg material up to fracture, the fractured portion continues to be forced against the die surface while undergoing plastic stretching, as highlighted by the yellow arrow. This allows additional deformation energy to be absorbed and compresses the previously stretched material, which remains attached to the AlSi10MnMg plate, as shown by the green arrow, resulting in localized adhesion and crushing of the region.

IV. CONCLUSION

The results demonstrate that, through the combined effect of high-quality high-recycled AlSi10MnMg alloy and optimized heat treatment, the microstructure and mechanical performance of high-pressure die-cast components can meet current requirements for automotive structural applications, supporting the development of lightweight and sustainable vehicles. The following key observations can be highlighted:

- The simulated paint-bake e-coating (EC) did not significantly alter the material properties, causing only minor changes to mechanical behavior, except for hardness, suggesting that under these parameters, EC cannot fully replace AA.
- Artificial aging (AA) treatment provided the highest YS and UTS.
- Annealing (AN) significantly improved ductility as confirmed by all mechanical tests performed.

It follows that, in industrial applications, the AN treatment makes the material suitable for components subjected to considerable deformation, such as automotive chassis and frames. In fact, high bend resistance offers flexibility for parts like shock towers and door beams, while increased rivet strength enhances performance in mechanical fastening during automotive assembly. In contrast, AA treatment ensures suitability for applications requiring maximum hardness and enhanced mechanical performance.

ACKNOWLEDGMENTS

Authors would like to acknowledge: Lauri L. and Bertoletti L. of Department of Mechanical and Industrial Engineering of University of Brescia (Brescia, BS, Italy), for acquiring the SEM images and drawing the specimen for tensile characterization, respectively. Mr. R. Zambelli and Raffmetal S.p.A. for providing the AlSi10MnMg alloy. Scaluggia N., Nolli E. and D'Angelo S. of Quality Department of Fondital S.p.A. a Socio Unico, for supplying the structural castings and conducting both bending and riveting tests.

FUNDING

Open access funding provided by Università degli Studi di Brescia within the CRUI-CARE Agreement. Financed by the European Union—NextGenerationEU (National Sustainable Mobility Center CN00000023, Italian Ministry of University and Research Decree n. 1033—17/06/2022, Spoke 11—Innovative Materials and Lightweighting). The opinions expressed are those of the authors only and should not be considered as representative of the European Union or the European Commission's official position. Neither the European Union nor the European Commission can be held responsible for them.

CONFLICT OF INTEREST

The authors declare that there are no conflicts of interest.

OPEN ACCESS

REFERENCES

1. M. Hirz and T.T. Nguyen: *World Electr. Veh. J.*, 2022, vol. 13(4), p. 61. https://doi.org/10.3390/wevj13040061.
2. H. Zhan, et al.: *J. Mater. Sci. Technol.*, 2023, vol. 154, pp. 251–68. https://doi.org/10.1016/j.jmst.2023.02.003.
3. D. Lehmhus: *Metals*, 2022, vol. 12(11), p. 1959. https://doi.org/10.3390/met12111959.
4. E. Mingotti, et al.: *J. Alloys Compd.*, 2025, vol. 1049, p. 185446. https://doi.org/10.1016/j.jallcom.2025.185446.
5. J. Gan, Y. Huang, C. Wen, and J. Du: *Trans. Nonferr. Met. Soc. China*, 2020, vol. 30(11), pp. 2879–90. https://doi.org/10.1016/S1003-6326(20)65428-0.
6. T. Trzepieciński and S.M. Najm: *Materials*, 2024. https://doi.org/10.3390/ma17030590.
7. S.-B. Kim, et al.: *J. Alloys Compd.*, 2022, vol. 906, p. 164339. https://doi.org/10.1016/j.jallcom.2022.164339.
8. R. Arcaleni, et al.: *Sustain. Mater. Technol.*, 2025, vol. 45, p. e01491. https://doi.org/10.1016/j.susmat.2025.e01491.
9. M.T. Alam and A. Ansari: *Int. J. Adv. Technol. Eng. Sci.*, 2017, vol. 5, pp. 278–94.
10. K. CharanNayak, A. Pathania, and A. RadhaPathania: *Mater. Today Proc.*, 2024. https://doi.org/10.1016/j.matpr.2024.05.026.
11. P. Krall, I. Weißensteiner, and S. Pogatscher: *Resour. Conserv. Recycl.*, 2024, vol. 202, p. 107370. https://doi.org/10.1016/j.resconrec.2023.107370.
12. L. Kuchariková, et al.: *Materials*, 2021. https://doi.org/10.3390/ma14081943.
13. X.Y. Jiao, et al.: *J. Mater. Sci. Technol.*, 2023, vol. 140, pp. 201–09. https://doi.org/10.1016/j.jmst.2022.09.014.
14. A.A. Luo, A.K. Sachdev, and D. Apelian: *J. Mater. Process. Technol.*, 2022, vol. 306, p. 117606. https://doi.org/10.1016/j.jmatprotec.2022.117606.
15. J.M. Sanchez, M. Arribas, H. Galarraga, M. Garcia de Cortazar, M. Ellero, and F. Girot: *Heliyon*, 2023, vol. 9(2), p. e13005. https://doi.org/10.1016/j.heliyon.2023.e13005.
16. E. Cinkilic, C.D. Ridgeway, X. Yan, and A.A. Luo: *Metall. Mater. Trans. A*, 2019, vol. 50A(12), pp. 5945–56. https://doi.org/10.1007/s11661-019-05469-6.
17. E. Cinkilic, M. Moodispaw, J. Zhang, J. Miao, and A.A. Luo: *Metall. Mater. Trans. A*, 2022, vol. 53A(8), pp. 2861–73. https://doi.org/10.1007/s11661-022-06711-4.
18. A. Niklas, S. Orden, A. Bakedano, M. da Silva, E. Nogués, and A.I. Fernández-Calvo: *Mater. Sci. Eng. A*, 2016, vol. 667, pp. 376–82. https://doi.org/10.1016/j.msea.2016.05.024.
19. M. Langseth, O.S. Hopperstad, and A.G. Hanssen: *Thin-Walled Struct.*, 1998, vol. 32(1), pp. 127–50. https://doi.org/10.1016/S0263-8231(98)00030-5.
20. J. Lu, et al.: *Metals*, 2021, vol. 11(4), p. 608. https://doi.org/10.3390/met11040608.
21. K. Anbalagan, R. Sarala, S.M. Sivagami, and S. Thamizhmanii: *Mater. Today Proc.*, 2023, vol. 90, pp. 123–27. https://doi.org/10.1016/j.matpr.2023.05.068.
22. J. Zhang and S. Yang: *J. Compos. Mater.*, 2014, vol. 49(12), pp. 1493–1502. https://doi.org/10.1177/0021998314535456.
23. Raffmetal S.p.a. https://www.raffmetal.it/alluminio-da-rifusione/leghe-alluminio-colata-continua#search.
24. F. Bachmann, R. Hielscher, and H. Schaeben: *Ultramicroscopy*, 2011, vol. 111(12), pp. 1720–33. https://doi.org/10.1016/j.ultramic.2011.08.002.
25. A.E. Salas Reyes, et al.: *J. Mater. Res. Technol.*, 2020, vol. 9(4), pp. 8266–82. https://doi.org/10.1016/j.jmrt.2020.05.098.
26. S. Ji, W. Yang, F. Gao, D. Watson, and Z. Fan: *Mater. Sci. Eng. A*, 2013, vol. 564, pp. 130–39. https://doi.org/10.1016/j.msea.2012.11.095.
27. N. Trometer, J. Zhang, Q. Wang, L. Wang, and A.A. Luo: *Int. J. Adv. Manuf. Technol.*, 2025, vol. 137(9), pp. 4825–37. https://doi.org/10.1007/s00170-025-15428-8.
28. G. Soares, et al.: *Metals*, 2023. https://doi.org/10.3390/met13020389.
29. E. Ogris, A. Wahlen, H. Lüchinger, and P.J. Uggowitzer: *J. Light Met.*, 2002, vol. 2(4), pp. 263–69. https://doi.org/10.1016/S1471-5317(03)00010-5.
30. P.D. Willenshofer, et al.: *Mater. Des.*, 2025, vol. 254, p. 114046. https://doi.org/10.1016/j.matdes.2025.114046.
31. G.D. Jiang, Y.H. Cai, C. Qiu, W.W. Zhang, and D.T. Zhang: *J. Mater. Res. Technol.*, 2022, vol. 21, pp. 3074–85. https://doi.org/10.1016/j.jmrt.2022.10.137.

32. K. Lee, Y.N. Kwon, and S. Lee: *J. Alloys Compd.*, 2008, vol. 461(1), pp. 532–41. https://doi.org/10.1016/j.jallcom.2007.07.038.
33. R. Liu, et al.: *Mater. Sci. Eng. A*, 2020, vol. 783, p. 139280. https://doi.org/10.1016/j.msea.2020.139280.
34. K. Lee, Y. Kwon, and S. Lee: *J. Alloys Compd.*, 2008, vol. 461, pp. 532–41. https://doi.org/10.1016/j.jallcom.2007.07.038.
35. G.E. Totten: *Hardness and Electrical Conductivity Testing of Aluminum Alloys*, ASM International, Materials Park, 2016.
36. X.Y. Jiao, et al.: *J. Mater. Process. Technol.*, 2021, vol. 298, p. 117299. https://doi.org/10.1016/j.jmatprotec.2021.117299.
37. Y.C. Lin, S.-C. Luo, J. Huang, L.-X. Yin, and X.-Y. Jiang: *Mater. Sci. Eng. A*, 2018, vol. 725, pp. 530–40. https://doi.org/10.1016/j.msea.2018.04.049.
38. A. Jarco: *Arch. Foundry Eng.*, 2017. https://doi.org/10.1515/afe-2017-0090.
39. B. Dalai, S. Jonsson, M. da Silva, L. Yu, and J. Kajberg: *Metall. Mater. Trans. A*, 2025, vol. 56A(1), pp. 196–218. https://doi.org/10.1007/s11661-024-07631-1.
40. Z. Hu, L. Wan, S. Wu, H. Wu, and X. Liu: *Mater. Des. (1980–2015)*, 2013, vol. 46, pp. 451–56. https://doi.org/10.1016/j.matdes.2012.10.020.
41. G.-H. Zhang, J.-X. Zhang, B.-C. Li, and W. Cai: *Prog. Nat. Sci. Mater. Int.*, 2011, vol. 21(5), pp. 380–85. https://doi.org/10.1016/S1002-0071(12)60073-2.
42. I. Katti, A. Jones, M. Weiss, D. Qiu, J.H. Forsmark, and M. Easton: *Rapid Prototyp. J.*, 2024, vol. 30(10), pp. 2145–60. https://doi.org/10.1108/RPJ-01-2024-0036.
43. C. Wang, Z. Du, A. Cheng, Z. He, H. Tan, and W. Yu: *J. Mater. Res. Technol.*, 2023, vol. 26, pp. 8857–78. https://doi.org/10.1016/j.jmrt.2023.09.187.
44. X. Zhao, D. Meng, J. Zhang, and Q. Han: *Int. J. Adv. Manuf. Technol.*, 2020, vol. 109(9), pp. 2409–19. https://doi.org/10.1007/s00170-020-05833-6.
45. Y. Liu, H. Li, H. Zhao, and X. Liu: *Int. J. Adv. Manuf. Technol.*, 2019. https://doi.org/10.1007/s00170-019-04567-4.
46. Y.C. Lin, M.-S. Chen, and J. Zhong: *Comput. Mater. Sci.*, 2008, vol. 43(4), pp. 1117–22. https://doi.org/10.1016/j.commatsci.2008.03.010.
47. Y.-C. Lin and M.-S. Chen: *J. Mater. Process. Technol.*, 2009, vol. 209(9), pp. 4578–83. https://doi.org/10.1016/j.jmatprotec.2008.10.036.